Geomorphology 356 (2020) 107088

Contents lists available at ScienceDirect

Geomorphology

journal homepage: www.elsevier.com/locate/geomorph

The use of a morphological acceleration factor in the simulation of large-scale fluvial morphodynamics

Jacob A. Morgan *, Nirnimesh Kumar, Alexander R. Horner-Devine, Shelby Ahrendt, Erkan Istanbullouglu, Christina Bandaragoda

Department of Civil and Environmental Engineering, University of Washington, United States of America

ARTICLE INFO

Article history:
Received 30 August 2019
Received in revised form 7 February 2020
Accepted 7 February 2020
Available online 18 February 2020

Keywords:
Numerical modeling
Morphological acceleration factor
Fluvial morphodynamics

ABSTRACT

Numerical simulation of fluvial morphodynamic processes can identify important dynamics at time and space scales difficult to observe in the field. However, simulations involving large spatial scales and/or the long time-scales characteristic of morphodynamic processes are often untenable because of long computation times. The morphological acceleration factor (morfac) applies a scalar multiplier to the sediment continuity equation, and is often applied in morphodynamic simulations to reduce computational time. Although the use of morfac in coastal simulations is relatively common, its applicability in field-scale fluvial models is generally confined to steady-flow simulations over reach-scale spatial domains. Here we explore the viability of using morfac to simulate large-scale, long-term morphodynamics in a gravel-bed river. We use Delft3D to simulate a 60-d period with a significant discharge event in the Nooksack River, Washington. We systematically adjust morfac values (ranging from 5 to 50) to compare with a baseline condition of no acceleration. Model results suggest that morfac-based modification of the inflow hydrograph time-series reduces peak flow magnitudes and flood wave celerities. Higher morfac values result in greater flood-wave attenuation and lower celerity, reducing the simulated morphological impact at locations farther downstream. In general, relative error compared to the model baseline increases farther downstream because of the altered flood-wave propagation. However, error analysis also shows a positive relationship with channel slope and a negative relationship with channel width; hence, errors increase in the steeper, confined reaches of the upper part of the domain. Even for the lowest morfac values absolute cumulative volume change errors are on the order of 10%, indicating that the use of morfac in fluvial simulations is best restricted to short-term and/or smaller-scale modeling efforts. Wider channel sections with lower gradients are shown to produce lower morfac-related errors. Therefore, morphological acceleration as examined here is potentially more appropriate for limited reaches rather than large-scale domains.

1. Introduction

Fluvial morphodynamics operate at large time ($\mathcal{O}$(10 yr)) and space ($\mathcal{O}$(10 km)) scales, but are typically governed by processes that occur at much smaller spatial and temporal scales. For example, Anderson and Konrad (2019) report basin-scale longitudinal profile adjustments of the Nooksack River to decade-scale climate fluctuations. The adjustments take the form of a bed material wave with a length scale of $\mathcal{O}$(10 km), propagating a distance of 90 km over a period of 50 yr. However, the sub-reach scale hydrodynamics and sediment transport processes that drive the propagation of the disturbance occur at much finer spatial and temporal scales. The range of scales makes numerical simulation difficult with large extents and fine resolutions both being necessary. In cases such as this, methods that reduce computational time are necessary for simulations to be made within research project timelines.

A morphological acceleration factor (morfac, M_f) is often used to reduce the computational time associated with long-term morphodynamic simulations. The morphological acceleration factor is a scalar quantity applied to the Exner's sediment continuity equation, assuming that morphodynamic evolution occurs at longer time scales than the hydrodynamic processes (Lesser et al., 2004). The use of M_f assumes a linear relationship between hydrodynamic and morphodynamic processes.

$$\frac{\partial \eta}{\partial t^*} = -\frac{M_f}{1-\lambda}\nabla \vec{q}_b \tag{1}$$

where η is the bed elevation, t^* is the effective time coordinate, λ is the porosity of sediment, and $\nabla \vec{q}_b$ is the divergence of the unit width bedload transport rate vector. The actual simulated time is $t = M_f \times t^*$. The magnitude of bed elevation change is increased by a factor of M_f (right hand

* Corresponding author.
E-mail address: jamor@uw.edu (J.A. Morgan).

https://doi.org/10.1016/j.geomorph.2020.107088

side of Eq. (1)), while time is decreased by a factor of M_f (left hand side of Eq. (1)). For simulations with steady inputs of water and sediment, M_f is applied by reducing the total simulation time by a factor of M_f and multiplying the divergence of the transport flux by M_f. For simulations with cyclic forcings, such as tides, each cycle simulated is assumed to represent M_f cycles. For unsteady, irregular forcings such as discharge hydrographs, the inflow time-series is manipulated by reducing the time values by a factor of M_f (e.g., Guerrero et al., 2015; Williams et al., 2016).

The morphological acceleration factor of $\mathcal{O}(100)$ has been frequently used in coastal and estuarine simulations (Lesser et al., 2004; van der Wegen and Roelvink, 2008; van der Wegen et al., 2008; Dastgheib et al., 2008). Explicit studies of how the value of M_f affects model results under different conditions have concluded that lower Froude numbers can generally accommodate higher M_f values (Li, 2010; Ranasinghe et al., 2011), and that higher M_f values generally underestimate the magnitude of morphological changes (Moerman, 2011). A time varying M_f has also been successfully used in multiple studies (e.g., Lesser, 2009; George et al., 2012; Stark, 2012). These studies have consistently concluded that the use and value of M_f should be evaluated on a case-by-case basis.

Although morphological acceleration factors are not uncommon in fluvial morphodynamic modeling, little systematic testing has been reported. In general, fluvial simulations that use M_f have steady discharge forcing or quasi-steady block hydrographs and M_f values of $\mathcal{O}(10)$ (Crosato et al., 2011; Edmonds, 2012; van Dijk et al., 2014; Singh et al., 2017), although some have used M_f values of $\mathcal{O}(100)$ (Kleinhans et al., 2008; Nicholas et al., 2013; Maaß and Schüttrumpf, 2018). However, the implications of using a morphological acceleration factor for simulations with natural flow variability and potentially large temporal discharge gradients are poorly understood (but see Williams et al., 2016).

In this paper we present a series of test simulations examining how the selection of a morphological acceleration factor affects modeled morphodynamic changes. The objective of this work is to identify how using morfac with altered hydrologic boundary conditions will affect predicted morphodynamics and to observe whether there are characteristic regions (e.g., similar channel slopes or widths) where morfac-related errors are minimized. To this end we perform several simulations of hydro- and morphodynamics in the Nooksack River, Washington, USA, with varying values of M_f and otherwise identical input parameters, and compare the resultant elevation change values. The model set-up, testing procedure, and evaluation procedure are described in Section 2. We present the results of the test simulations and their evaluations in Section 3. We discuss these findings and additional considerations in Section 4, and provide a summary and conclusion in Section 5.

2. Methods

2.1. Depth-averaged morphodynamic model

We use Delft3D (4.03.01) in a depth-averaged, two-dimensional implementation to investigate the effect a morphological acceleration factor has on simulation morphodynamics. Delft3D solves the Reynolds-averaged Navier Stokes equations, in this case, simplified with the shallow water and Boussinesq approximations (Lesser et al., 2004; Deltares, 2014).

2.2. Model set-up

Our model simulates the Nooksack River in northwestern Washington State, USA (Fig. 1). The modeling domain covers approximately 80 km of river length, which includes two major tributaries: the Middle Fork Nooksack River at $s \approx 25$ km and the South Fork Nooksack River at $s \approx 30$ km, where s is the streamwise distance downstream from the upstream boundary. The upstream boundary of the domain is located approximately 10 km downstream of USGS gage 12205000 North Fork (NF) Nooksack below Cascade Creek near Glacier, WA (at an elevation of approximately 250 m, Fig. 2a) and the downstream boundary is located at USGS gage 12213100 Nooksack River at Ferndale, WA. The mainstem Nooksack within the modeling domain has mean channel slopes up to 1.5% (Fig. 2b), surface sediment diameters ranging from very coarse sand to cobble (Fig. 2c), and reaches that alternate between single thread and braided (relatively narrow and wide channel widths, Fig. 2d). Under low flow conditions (12 m3/s in the NF), Froude numbers are generally subcritical with reach-averaged values varying from 0.5 to 0.25 (Fig. 2e). Within the lower 25 km of the domain (s>55 km) the channel is confined by levees. For the set of simplified simulations presented in this paper, we did not parameterize levee location or height beyond the interpolated initial elevations (discussed more below).

We used the Alternating Direction Implicit (ADI) method for temporal discretization of unsteady, shallow water hydrodynamics and Delft3D's default cyclic scheme for spatial discretization. Bedload transport was simulated using the Wilcock and Crowe (2003) formula, which allows for the specific transport of multiple grain size classes and their interactions (e.g., hiding and protrusion). Six grain size classes were specified for the simulations, ranging from very fine sand to boulders. The deposition and exhumation of stratigraphic layers was represented using Delft3D's Underlayer option. The transport layer was specified as 10% of the water depth. We allow a maximum of five layers with a maximum layer thickness of 0.3 m. Surface roughness was parameterized

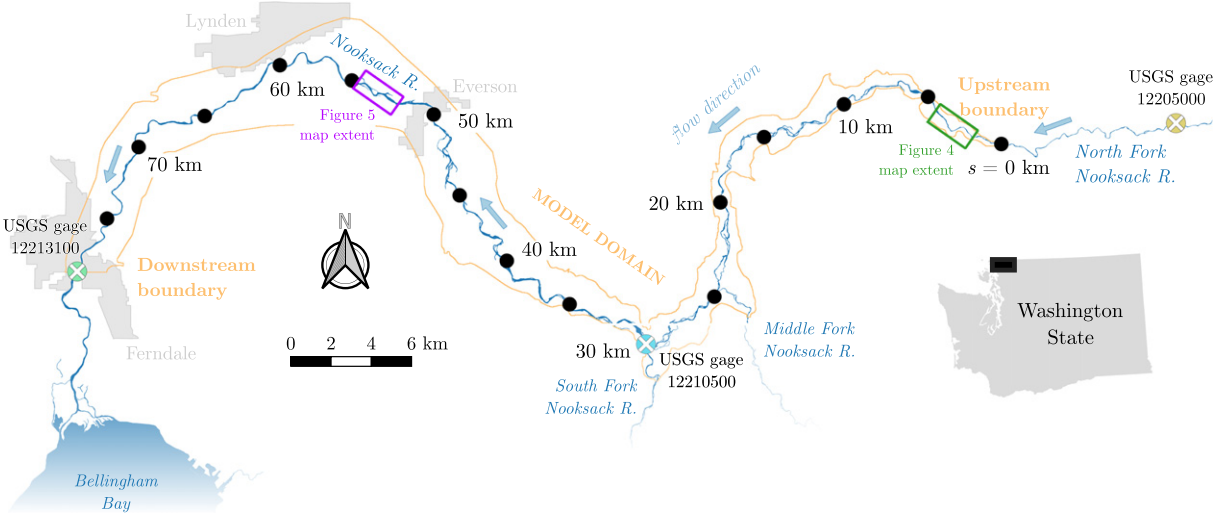

Fig. 1. Simulation domain of the Nooksack River in northwestern Washington State with labels of the streamwise distance, s, downstream from the upstream boundary (s=0 km). Map extents are shown for Fig. 5 (s=2 − 4 km) and Fig. 6 (s=53 − 55 km).

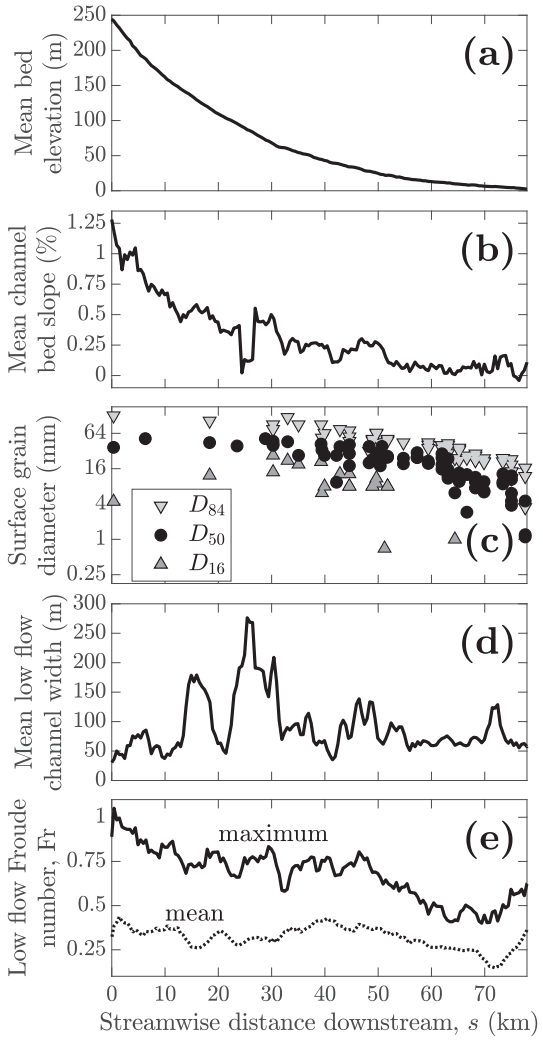

Fig. 2. Channel characteristics of the mainstem Nooksack River within the modeling domain including: (a) longitudinal profile of mean bed elevations; (b) mean channel slopes averaged over 0.5 km intervals; (c) measured grain sizes within the model domain from sources referenced in the text; (d) low flow (initial) mean wetted channel widths; and (e) low flow mean and maximum Froude numbers. This figure illustrates the range of slopes and channel widths within our simulation domain. Regions of relatively low local channel slope and high width values (e.g., s=25 km) correspond to unconfined valley sections where the channel planform generally takes a braiding pattern.

using the Nikuradse roughness length. A friction coefficient is computed from the Nikuradse roughness length using the White-Colebrook formula (Colebrook and White, 1937; Colebrook, 1939). We use a steady, non-uniform Nikuradse roughness length specified as three times the initial surface D_{84} (where D_{84} is the diameter for which 84% of the surface sediments are finer). Initial surface grain sizes are explained below. Spiral flow effects on the momentum were parameterized using the method of Kalkwijk and Booij (1986) with a correction coefficient of 0.5 (see Deltares (2014) for more details). Transverse slope effects were considered using the default method of Ikeda (1984) with a coefficient of 1.5 (see Deltares (2014) for more details). No bank erosion processes were explicitly parameterized. A grid of square cells was specified over the modeling domain to include the channels and adjacent floodplains (Fig. 1) with grid spacing of $\Delta x = \Delta y$=20 m. For 80% of reaches in the domain this corresponded to at least three grid cells across the low flow active channel width and 25% of reaches are represented by at least five grid cells across the width (Fig. 2d). The relatively low cross-channel resolution is reasonable for the simulations considered here, as the cross-channel effects of morphological evolution are not particularly focused on. To accommodate the grid spacing and simulated flow velocities, we used a time step of Δt=0.05 min =3 s, resulting in a maximum Courant number of Cr=0.81.

The initial conditions were generated using the following spatial information: channel bathymetry, floodplain topography, grain size distributions, and a 30-d initial flood simulation. Channel bathymetry and floodplain topography were interpolated from lidar measurements where available. Lidar data were collected for our area of interest in January 2013 (WSI, 2013). Bathymetry data for Ferndale (s=80 km) upstream to Everson (s=50 km) were collected in August 2015 using a boat-mounted ADCP coupled with RTK-GPS (Anderson and Grossman, 2017). These two datasets were combined to create a continuous elevation map (including bathymetry from Ferndale to Everson). During lidar acquisition the estimated average flow depth upstream of Everson is 1 m. Therefore, upstream of Everson, the water surface from the lidar DEM was hand delineated and raster cells were reduced in elevation by 1 m, essentially assuming a uniform water depth of 1 m. The combined topo-bathymetry elevation model was coarsened to the numerical grid spacing of 20 m through averaging. Before test simulations a 30-d initialization simulation was performed to "naturalize" the discordant bathymetry, which resulted in the initial topo-bathymetry used for our morfac testing simulations. Because the region shows high morphodynamism, no attempt was made to arrive at any sort of morphodynamic equilibrium during the initialization.

The initial spatial pattern of grain size distributions were estimated using previous surface measurements dating back to the 1970s (Collings et al., 1972; Westbrook, 1987; Northwest Hydraulics Consultants, 1989; Bertschi, 1993; KCM, Inc., 1995) (Fig. 2c). Power-law models were fit to the longitudinal location and measured values of D_{16}, D_{50}, and D_{84}. Grain size maps were created by first separating the modeling domain into two regions: historically active channel and floodplain. We used geospatial data generated by Collins and Sheikh (2004), which delineate active channel areas dating back to the early 1900s. The power-law models of characteristic grain sizes were used to create distributions (using the grain size classes mentioned above) at equal spatial intervals along the longitudinal direction of the active channel. Adjacent floodplains (areas inside the domain, but outside the active channel area) were assigned distributions with diameters half of the active channel. The floodplain grain diameters in the field are not known explicitly, but finer grains are consistent with the glacial sediments common to the Puget Lowlands, and we assume our formulation captures that general trend.

We performed an initializing simulation to account for the limited spatial extent of field data and the assumptions made in creating initial topo-bathymetry and grain size distributions. The simulation was comprised of a single significant flow event with a duration of 30 d (the same event used in the test simulations and described below). During this simulation no sediment was supplied to the boundaries, but the bed morphology within the domain was allowed to adjust through elevation changes and grain sorting. The final conditions of this preliminary simulation constitute the initial conditions for each of our test simulations.

2.3. Testing procedure

Our focus is on a series of seven simulations, with M_f values of 1, 5, 7.5, 10, 15, 20, and 50. In these simulations a single upstream boundary is used, the North Fork Nooksack River. Although USGS stream gage measurements exist near the upstream boundary (Fig. 1), the benefit of their use as a boundary condition is negated by the presence of major tributary contributions within the domain, where timing and magnitudes of flow are not measured. The downstream-most gages on each of the two major tributaries are located kilometers from the respective confluences with the mainstem river. Therefore, water discharge was specified from the distributed hydrological model Topnet-WM (Bandaragoda et al., 2012, 2019). Topnet results corresponding to the location of s=0 km were used as the upstream discharge boundary

condition. Although Topnet model output also includes computed streamflow for the Middle Fork and South Fork, discharge contributions from these, and other more minor, tributaries were not considered. A sixty day period covering October–November 2003 was selected as it spanned a historically significant event with a maximum discharge of approximately 300 m3/s, corresponding to an estimated 18-yr recurrence interval at the North Fork USGS gage station (see Fig. 4a, s=0 km). Starting from approximately s=30 km and downstream to the mouth, a 300 m3/s event corresponds < 1-yr recurrence interval. For all of our simulations, no sediment was supplied through the upstream boundary.[1] Downstream boundary conditions (Ferndale) were specified using a stage-discharge curve derived from recent measurements at USGS gage 12213100 (U.S. Geological Survey, 2018). At the downstream boundary, the bed elevations and surface grain sizes were able to freely evolve. However, the stage-discharge relationship was held constant throughout the simulation. It is likely boundary effects influenced the domain in the region of the downstream boundary, which is consistent with other similar studies (Duró et al., 2016). Therefore, the 10 km closest to the downstream boundary were not considered in our analysis.

For each simulation, the inflow boundary hydrographs were altered by dividing each time value in the time-series by M_f. Because the computational timestep remains the same, this reduces the total simulation time by a factor of M_f. For analysis of simulation results we normalize output times by M_f to obtain corrected times.

2.4. Evaluation procedure

To determine how M_f affects hydro- and morphodynamic results, we compare runs with M_f>1 to a base case run with no morphological acceleration (M_f=1). Hydrodynamics are compared by considering the effect of hydrograph compression on flood wave propagation and attenuation (Mosselman and Le, 2016). For this, we compare the celerity of the flood wave as well as the relative peak discharge magnitude at several monitoring locations along the longitudinal profile of the mainstem. Morphodynamics are compared by considering the differences in elevation changes throughout the simulation domain. For these comparisons we use the percent error in test simulations relative to the base simulation. For a parameter P, the percent error of that parameter E_P, can be computed

$$E_P = 100\times \left| \frac{P_{test} - P_{base}}{P_{base}} \right| \quad (2)$$

where subscripts *test* and *base* correspond to parameter values from test and base simulations, respectively.

2.5. Model corroboration with observational data

This study explores the effects of reducing computational time by using a morphological acceleration factor and hydrograph compression. The model simulations are therefore intended to replicate the key fluvial morphodynamic processes in a gravel bedded river at the event time-scale, and can only be validated qualitatively. Because we do not use observed discharge for our upstream boundary conditions, a one-to-one comparison with gage station measurements is not possible. However, the qualitative accuracy of base simulation hydrodynamics is determined by comparing modeled floodwave celerity to those calculated from field measurements in the lower Nooksack. The cross-correlation between instantaneous discharge data at USGS gage stations 12210500 and 12213100 from 1997 to 2002 (U.S. Geological Survey, 2018) was used to estimate the time lag between stations (David et al., 2011). We calculated time lags associated with maximum cross-correlation coefficients over the time period using a 14-d moving window with 50% overlap between windows (Fig. 3a). The celerity is calculated as the distance between the two stations (≈50 km) divided by the time lag (Fig. 3b). The mean of estimated celerities is 9.2 km/h, while the median is 7.1 km/h. Our simulated average celerity of 7.5 km/h for the base simulation reasonably agrees with the estimated distribution from gage measurements (Fig. 3b).

A direct comparison of simulated morphodynamics and field observations is also difficult given that our base simulation does not correspond to a monitored event. Additionally, bedload transport observations are limited in both space and time and elevation change data, derived from lidar differencing, spans multi-year time intervals (Anderson et al., 2019). Specific gage analysis shows variations in bed elevations on the order of $\mathcal{O}$(1 m) at USGS gage stations along the mainstem (Anderson and Konrad, 2019; Anderson et al., 2019). At the event time-scale, stage residuals vary by up to 1 m at the North Fork gage and up to 0.2 m at the Ferndale gage (Anderson and Konrad, 2019). Modeled total elevation changes vary from maximum absolute values of 1.2 m in the upper part of the domain to 0.1 m in the lower part of the domain, and therefore compares well with this specific gage data. Median non-zero elevation change values vary from 0.2 m in the upstream to 0.01 cm in the downstream. These values are consistent with the order of magnitude of changes observed in the specific gage analysis for these regions (Anderson and Konrad, 2019).

3. Results

The implementation of a morphological acceleration factor as we have used it here requires modification of the inflow hydrograph, effectively compressing the hydrograph by reducing each time reference by a factor of M_f. The attenuation (diffusivity) of a flood wave is largely

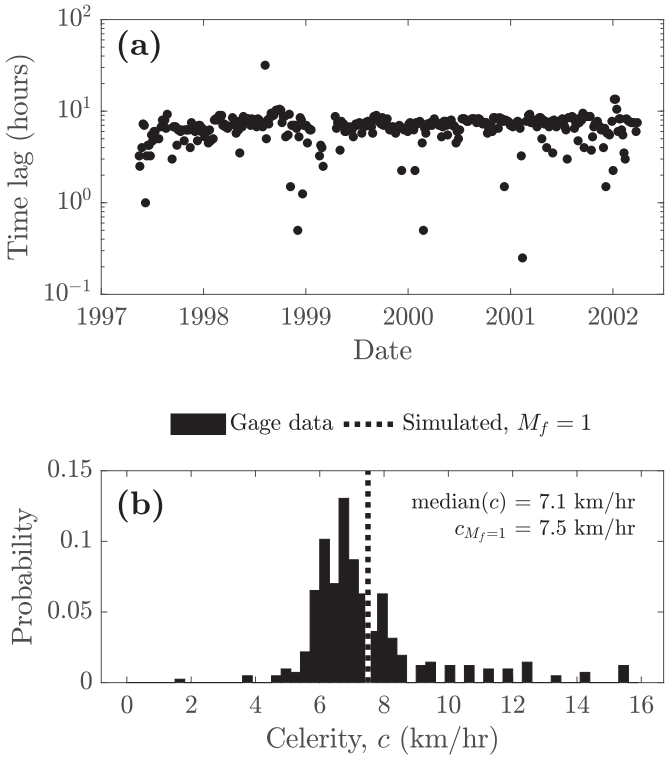

Fig. 3. (a) Time lag between observed hydrographs at USGS gages 12210500 (Deming, $s \approx 30$ km) and 12213100 (Ferndale, $s \approx 80$ km). (b) Histogram of floodwave celerity computed from time lag between observed hydrographs compared with the simulated celerity from the base simulation (M_f=1).

[1] It is theoretically possible to add sediment supply from the upstream boundary, however, our modeling efforts rely on parallel computing techniques, for which non-default morphological boundary conditions are not compatible (Bert Jagers, Deltares, personal communication).

influenced by the timing (period, or time to peak) and magnitude of the inflow hydrograph (Fenton, 2019). Therefore, we first present the effect of M_f on the propagation of the flood wave and then present the differences in calculated morphodynamics.

3.1. Flood wave propagation

For the discharge event included in our simulations the peak flow at the upstream boundary is 295 m^3/s and occurs at t_c=20 d (Fig. 4a), where t_c is the corrected time calculated as the simulated time multiplied by M_f. For M_f=1 the time-series hydrograph retains its shape and decreases in magnitude by only 4 m3/s as the flood wave propagates downstream and eventually exits the domain at the downstream boundary, where the peak discharge occurs 16.5 h later at t_c=20.7 d (Fig. 4b and e). Excluding the downstream-most 10 km, because of boundary effects, the simulated flood wave for M_f=1 had a consistent approximate celerity of c=2 m/s. The M_f=1 reference flood wave has negligible diffusion (Fig. 4a), which is consistent for longer events in steeper channels (Fenton, 2019).

The upstream boundary hydrograph compression associated with our use of morfac results in consistently more attenuative discharge hydrographs with higher morfac values. Although the inflow hydrograph is identical in corrected time for every simulation (Fig. 4a), the inflow hydrograph as actually implemented has time intervals that are $1/M_f$ that of the corrected time. This compression of inflow hydrograph time-series creates steeper rising and falling limbs, which in turn produce more dispersive discharge waves (Fig. 4a). Higher values of M_f consistently result in lower peak discharge magnitudes and greater time lags relative to M_f=1.

Flood wave celerity decreases with increasing morfac (Fig. 4b–d), and the nonlinear flood wave propagation and feedback with channel morphodynamics is considered here. The relative timing and position of the flood wave in all simulations show a power-law-type relationship, $s_Q = \alpha t_Q^{\beta}$, where s_Q is the distance downstream of the monitoring location, t_Q is the time that the peak discharge occurs at the monitoring location, α is the power-law constant, and β is the power-law exponent. Exponents are slightly lower than unity, suggesting slight reductions in celerity as the flood wave propagates downstream. The exponent for M_f=1 was close to unity, and was slightly lower for higher morfac values, ranging from 0.85 to 0.95 (Fig. 4d). More significantly, the power-law constants, α, decrease significantly with the use of higher morfac values as $\alpha = 180 \times M_f^{-0.9}$ (Fig. 4c). If we take $\beta \approx 1$, then α is essentially the celerity in km/d. Values of α range over nearly two orders of magnitude, from 2 m/s for M_f=1 to 0.06 m/s for M_f=50 (Fig. 4c). The celerity of the flood waves can be formulated as the time derivative of the downstream position, $c = ds_Q/dt_Q = \alpha\beta t_Q^{\beta-1}$. In these results, M_f inversely scales celerity as $c \approx 180 \times M_f^{-1}$, resulting in slower floodwave propagation with increasing M_f.

The rate of flood wave magnitude reduction also increases with increasing morfac (Fig. 4e). While the peak discharge for the M_f=1 simulation decreased by approximately 1%, the peak discharge for the M_f=50 simulation had decreased by approximately 25% at the downstream end of the domain. When simulation times are corrected by multiplying timestamps by M_f the discharge reduction (ΔQ) versus relative corrected time data collapse into a consistent linear trend, $\Delta Q = 4.2 \times t_Q$ (Fig. 4f). Greater reduction in peak flood magnitude with morfac is likely a combination of the decreased flood volume as well as the increased temporal discharge gradients at the boundary, both effects of the hydrograph compression. Again taking β=1, the reduction in peak discharge can be seen to be approximately proportional to both the downstream distance and the morfac, $\Delta Q \approx 0.02 \times s_Q \times M_f$.

3.2. Morphodynamic changes and differences

Examples showing the net elevation changes over the entire simulated period are shown for an upstream and downstream reach of the domain in Figs. 5 and 6, respectively. Net erosion and deposition occurs in similar areas for each morfac simulation. However, the amount of erosion and deposition generally decreases as M_f increases (Figs. 5a–g

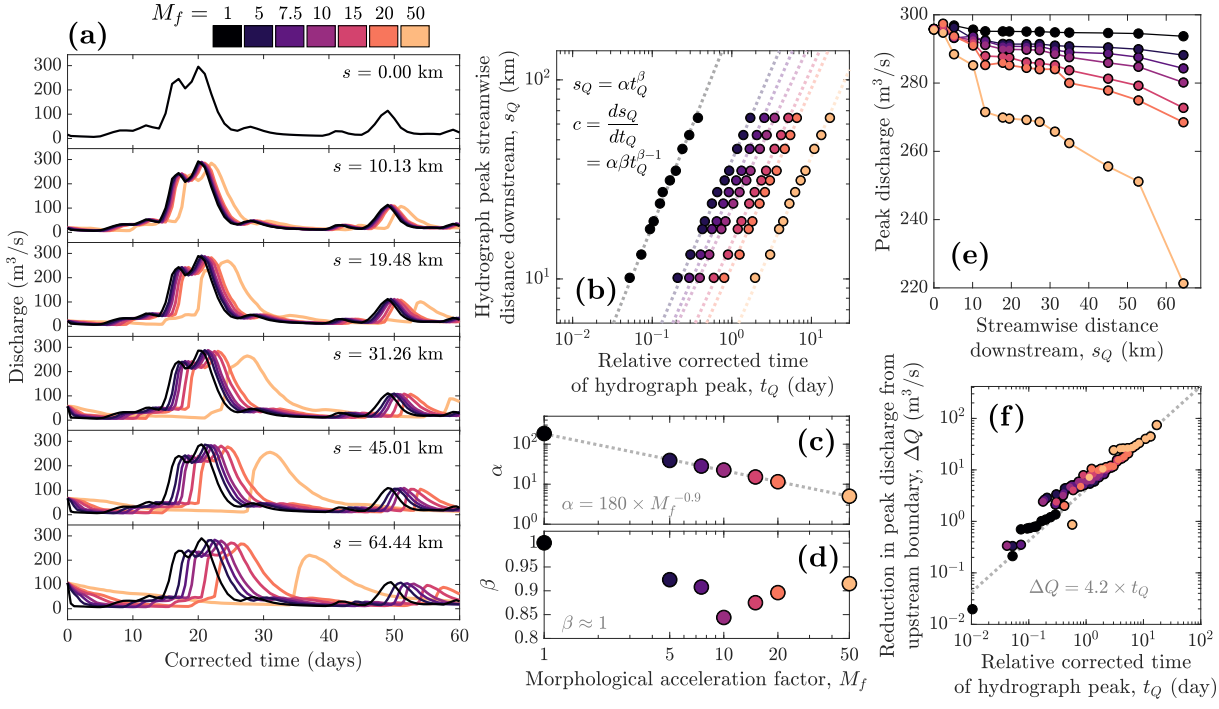

Fig. 4. Flood wave propagation and attenuation (without tributary flow contributions) effects shown by (a) time-series discharge at several downstream locations, (b) relative position and timing of peak discharge including power-law fits, (c) and (d) exponent and coefficient values for power-law fits of s_Q as a function of t_Q in relation to M_f, respectively, (e) peak discharge magnitude at downstream monitoring cross sections, and (f) reduction in peak discharge against relative corrected time with a linear fit. Colors corresponding to specific M_f values are consistent in all subplots.

and 6a–g). Certain regions of the domain show thalweg erosion and adjacent floodplain deposition (Fig. 6). However, such a pattern is not ubiquitous and on the order of centimeters. In other areas (e.g., Fig. 5) there is apparent meander migration with deposition occurring on bars opposite eroding bank slopes. Generally the magnitude of error between test morfac simulations and the base is greater in areas of greater morphological change (Figs. 5h–m and 6h–m). Absolute percent errors in total elevation change for each simulation range from 0 to ≥ 100, with higher M_f values corresponding to overall higher percent error values (Figs. 5n–s and 6n–s).

To evaluate longitudinal variability in morphodynamic results, we combine morphodynamic changes and associated errors over reaches of Δs=0.5 km length in the stream-wise direction (Fig. 7). Changing Δs by a factor of two does not change the findings in this section. Directional trends in elevation changes are again consistent between test simulations, with results showing similar regions of high/low magnitudes of positive and negative volume changes (Fig. 7a–g). Magnitudes generally diminish with higher M_f values. Net summed elevation changes over Δs intervals also show similar trends in both direction and relative magnitude. Elevation change errors for these intervals range from less than 1% to greater than 100%, with errors generally increasing with M_f (Fig. 7h–m). Signed and net errors both show consistent spatial patterns between test simulation results, with coincident areas of relative high or low errors. For example, at approximately s=39 km, M_f=5 results show a region of relatively high error (~30%, Fig. 7h), which remains a region of high error for increasing M_f values, increasing to an error of ~700% for M_f=50.

We can additionally summarize the morphodynamic changes by combining the morphodynamic results over the whole domain and for the entire simulation period. The median percent error in cumulative net elevation change increases with M_f as a power-law function: $\overline{E_{p,\eta}} = 0.022(M_f - 1)^{0.71}$ (Fig. 8). The power-law exponent is less than unity, indicating that as M_f increases, relative median errors throughout the entire domain increase at a slower rate. This suggests that an increase in a low value morfac results in disproportionately larger errors than the same increase in a high value morfac. By summing net elevation changes and multiplying by the cell size we can obtain total volumetric changes over the simulated time (Table 1). Higher M_f values correspond to lower magnitudes of both total positive and total negative volume changes, resulting in differences of total net volume changes that increasingly depart from the reference simulation (M_f=1) as M_f increases. Percent errors in total positive and total negative volume changes both trend with morfac according to $E_{P,V}$=0.07$(M_f - 1)^{0.33}$, where $E_{P,V}$ is the absolute percent error in total volume change. Absolute percent error in total net volume change monotonically increases with M_f, ranging from 8% for M_f=5 to 30% for M_f=50 (Table 1).

Texture of the surface material showed little difference between simulations with different M_f values. Although minor local differences occur, related to the magnitude and direction of elevation change both at that location and the locations upstream, average grain size statistics at 0.5 km steps show negligible differences. This may be caused by a slowing of sorting process time-scales associated with the use of morfac (Chavarrías et al., 2019). Alternatively, it may suggest that initial grain size conditions are more important than the effects of the value of M_f,

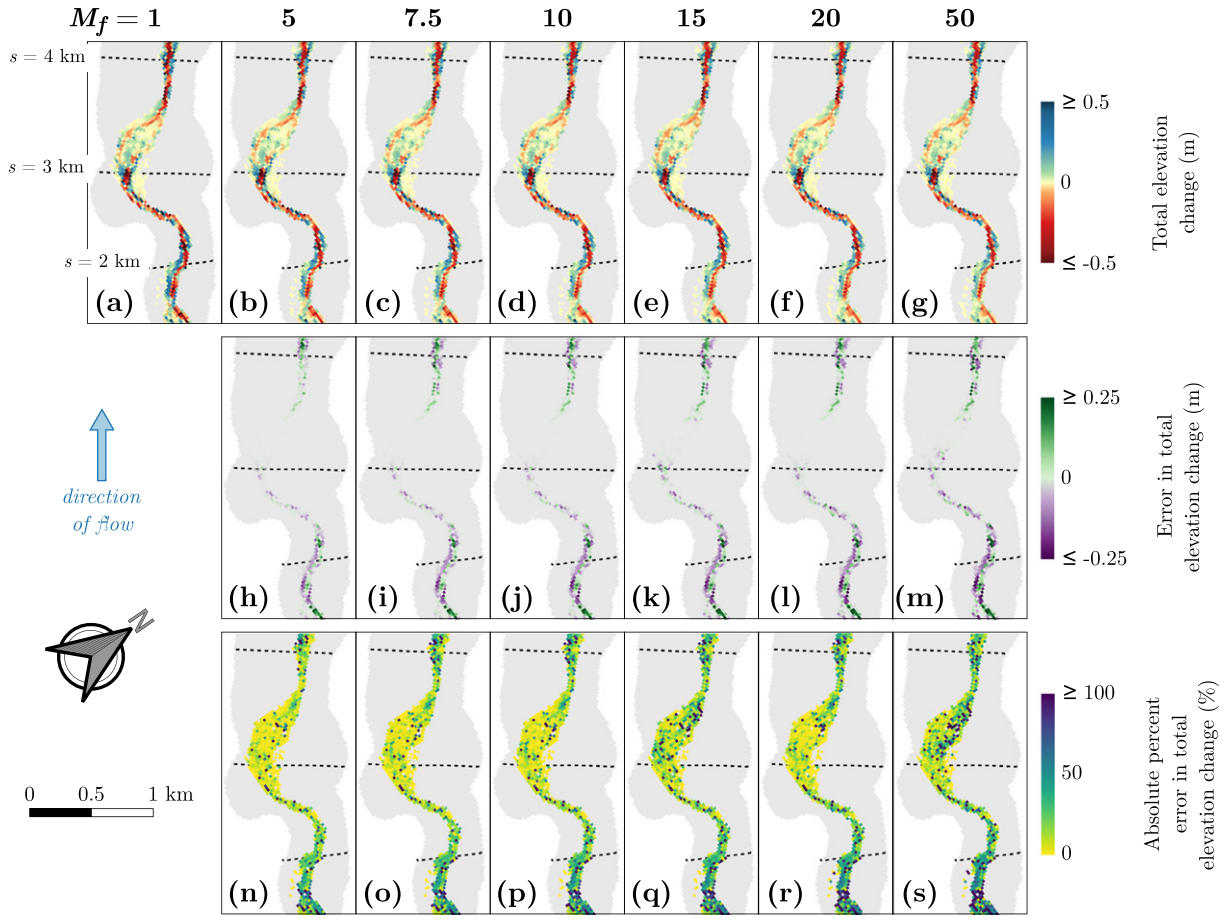

Fig. 5. Example output result maps from an approximately 3 km reach near the upstream NF Nooksack boundary. (a–g) Total net elevation changes over the entire simulation period. (h–m) Error in the total net elevation changes relative to M_f=1. (n–s) Absolute percent error in the total net elevation changes relative to M_f=1.

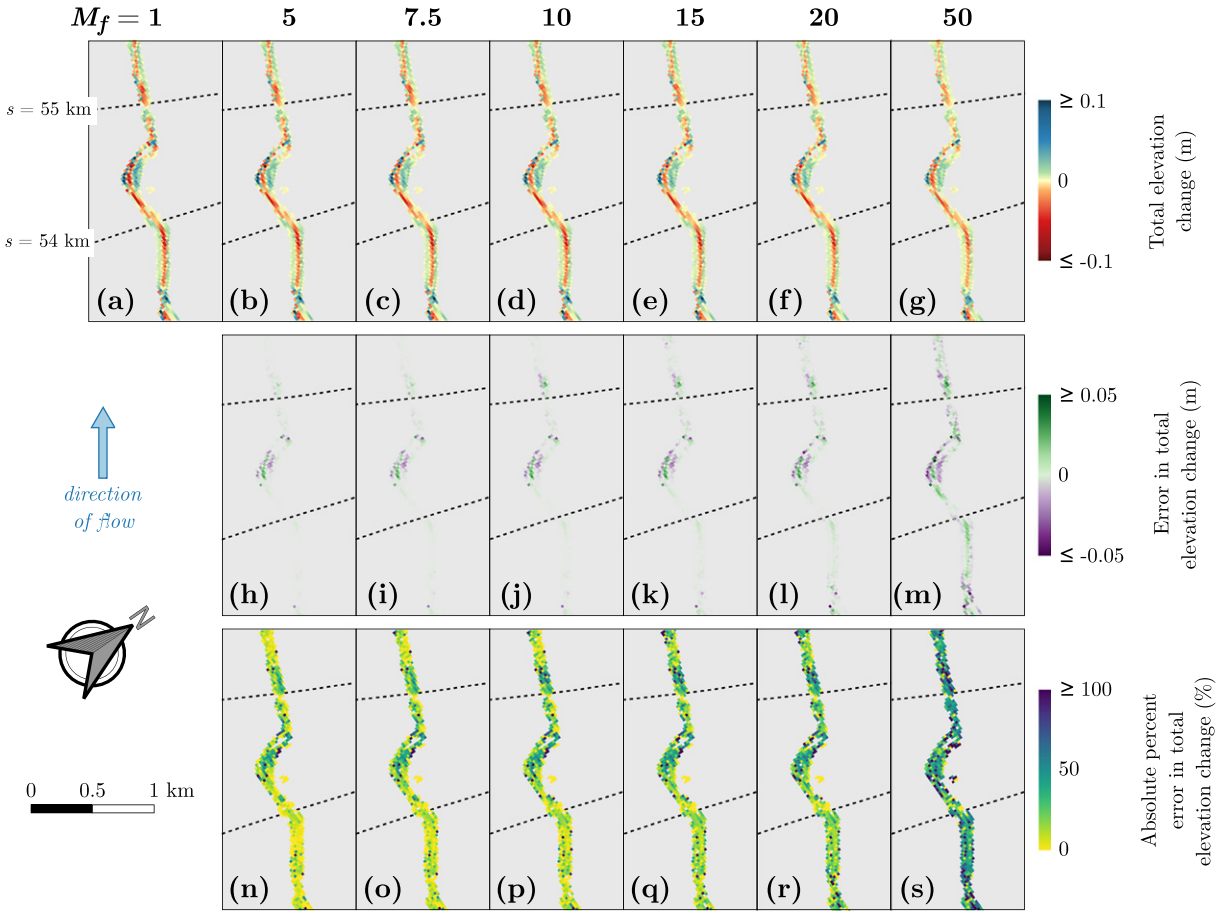

Fig. 6. Example output result maps from an approximately 3 km reach near the downstream boundary. (a–g) Total net elevation changes over the entire simulation period. (h–m) Error in the total net elevation changes relative to M_f=1. (n–s) Absolute percent error in the total net elevation changes relative to M_f=1.

or that the simulation time was simply too short and precluded substantial evolution of surface texture.

4. Discussion

The results presented in the previous section show that increasing M_f generally results in increases in errors of computed elevation changes, both locally and domain-wide. In this section, we discuss how flood-wave propagation affects morphological errors (Section 4.1), how errors are organized spatially (Section 4.2), and how the addition of contributing flow from major tributaries affects morfac-related errors (Section 4.3). Additionally, we discuss issues surrounding the extrapolation of our findings to longer time-scale simulations (Section 4.4). Finally, we summarize other time-saving methods that draw on the morphological acceleration parameter and concept (Section 4.5).

4.1. Effect of altered hydrodynamics on morphodynamics

Compressing the upstream boundary hydrograph by a factor of M_f results in a more attenuative flood wave, reducing discharge magnitudes at downstream locations, and resulting in greater morphological errors with increasing M_f. Increased flood wave diffusion is predictable given a higher temporal gradient in upstream boundary discharge (Fenton, 2019) and this effect from using a compressed hydrograph has been observed (Williams et al., 2016). We found a two-fold effect on morphodynamics caused by discharge magnitude reduction. First, lower discharges result in lower shear stress values, reducing the overall potential for geomorphic work, resulting in muted morphodynamics. Second, lower discharges result in a reduced spatial extent of wetted cells. These two factors together result in two related types of errors. First, errors result when the test simulation underpredicts morphological changes relative to the base. Second, errors arise when the base simulation predicts changes but the test simulation does not, either because the cell was not inundated or was inundated but did not have sufficient shear stress to mobilize the surface material. These effects on morphodynamics caused by hydrodynamics are illustrated when we define morphologically active cells as grid cells with a non-zero elevation change over the simulation (Fig. 9). A relationship exists between both morfac values (Fig. 9a) and the resultant errors (Fig. 9b). The percent errors in the number of morphologically active cells remain relatively small (≤4%). However, these relatively small errors propagate into elevation errors that are an order of magnitude greater (Fig. 9b). For example, a 4% error in the number of morphologically active cells in M_f=50 corresponds to a 37% median error in elevation changes (Fig. 9b).

4.2. Spatial variability of morphodynamic errors

Interactions between discharge and channel characteristics (slope, width, etc.) result in potentially complicated hydrodynamics, which are also altered by our implementation of morfac. Downstream variations in errors show consistent patterns across M_f values (Fig. 7h–m), suggesting that morphodynamic errors are influenced by local channel conditions as well as M_f value. For example, although discharge magnitude errors increase in the downstream direction, each test simulation shows a general decrease in errors in the 25 km immediately downstream from the upstream boundary (Figs. 7h–m and 10a). The coupled influence of morfac and channel geometry on resultant errors is

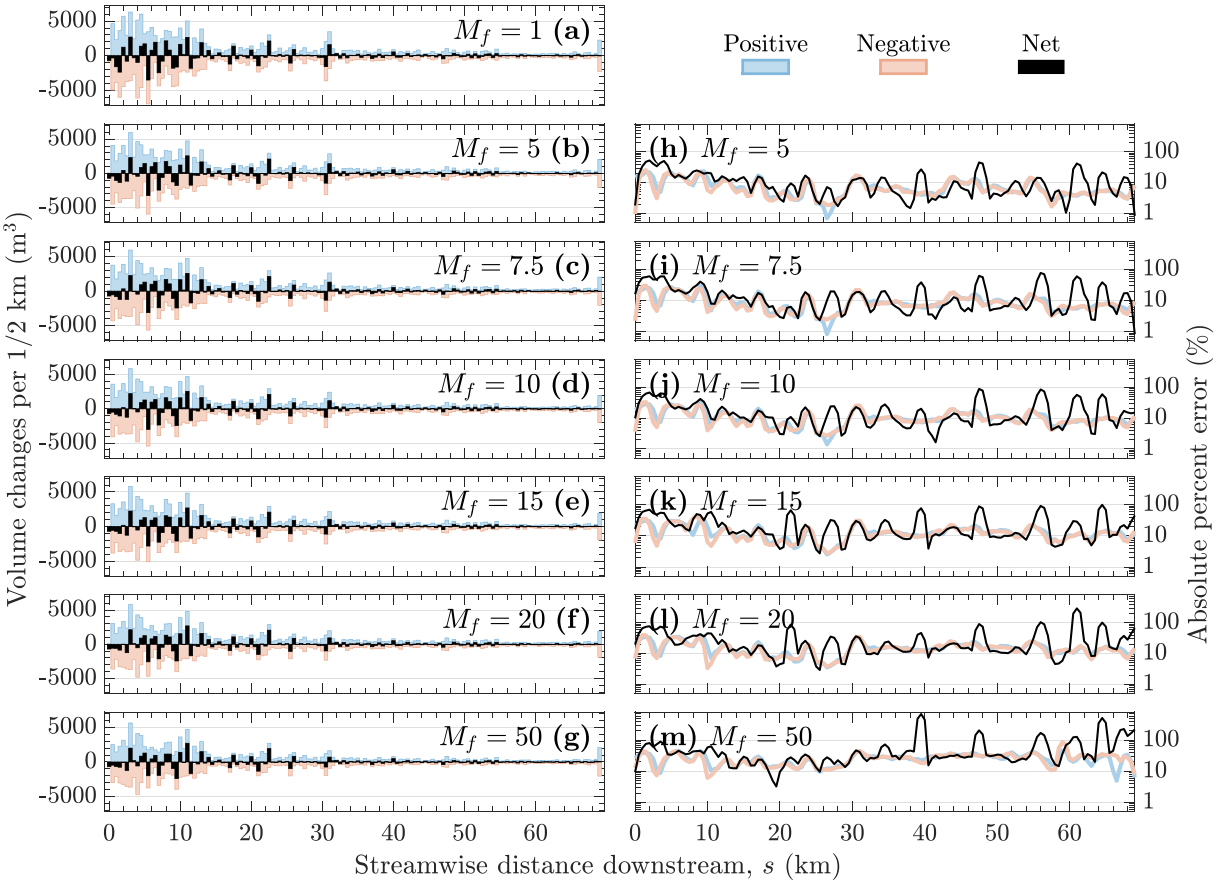

Fig. 7. (a–g) Volume changes within each 1/2 km of the stream-wise length. (h–m) Absolute percent errors for volume changes. Errors plots are displayed using a LOWESS smoothing filter with a window of 5.

confounded because channel geometry parameters, such as slope and width, vary simultaneously and without systematic organization. For example, channel slope and width are related, but do not always vary consistently. In general, higher M_f values result in greater errors (Fig. 10a). However, the range of errors for a single M_f is as much as the range of errors between M_f simulations for a specific location. The range of errors at s=9.5 km in Fig. 10a is as much as the range of errors in only M_f=5 from s= 8 to 11 km. These distinct downstream patterns suggest that channel geometry is a primary control on resultant errors (Fig. 10b). Errors show a generally positive trend with channel slope (Fig. 10c) and a generally negative trend with channel width (Fig. 10d), indicating that conditions leading to greater shear stresses result in larger magnitude errors. Others have noted that using morfac with greater Froude numbers results in greater errors (Li, 2010), which is consistent with this assessment (Fig. 10c and d). Farther downstream (s>30 km) channel slopes and widths show less variation (Fig. 2).

Absolute percent errors in total positive and negative volume changes presented here range from 11% (M_f=2) to 26% (M_f=50) (Table 1), which are similar to the values reported by Williams et al.

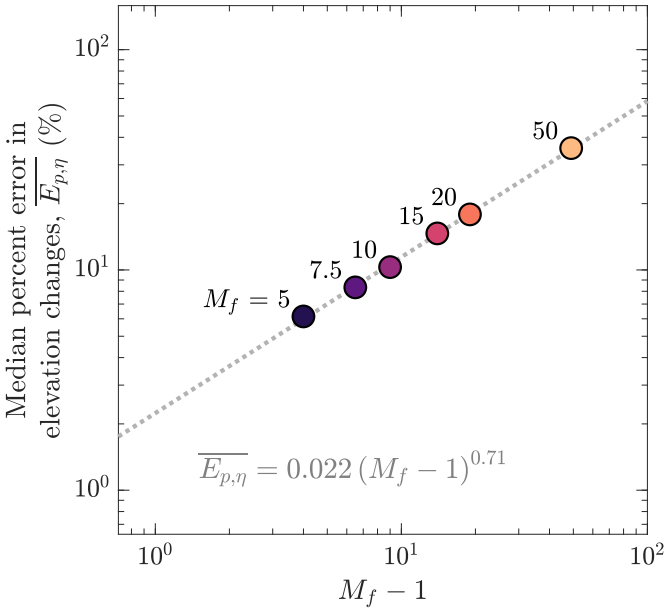

Fig. 8. Increase of median percent error in net elevation changes with morfac. The dotted line corresponds to the power-law function $\overline{E_{p,\eta}} = 0.022(M_f - 1)^{0.71}$.

Table 1
Total volume changes integrated over space and time for each simulation without tributary flow contributions and associated errors relative to morfac=1.

morfac, M_f	Total positive volume change (m^3)	Total negative volume change (m^3)	Total net volume change (m^3)	Absolute percent error in total net volume change (%)
1	163,272	−163,340	−68	0
5	144,808	−144,870	−62	8
7.5	141,106	−141,188	−82	20
10	138,350	−138,432	−82	21
15	135,205	−135,290	−84	24
20	131,179	−131,265	−86	26
50	120,375	−120,464	−89	30

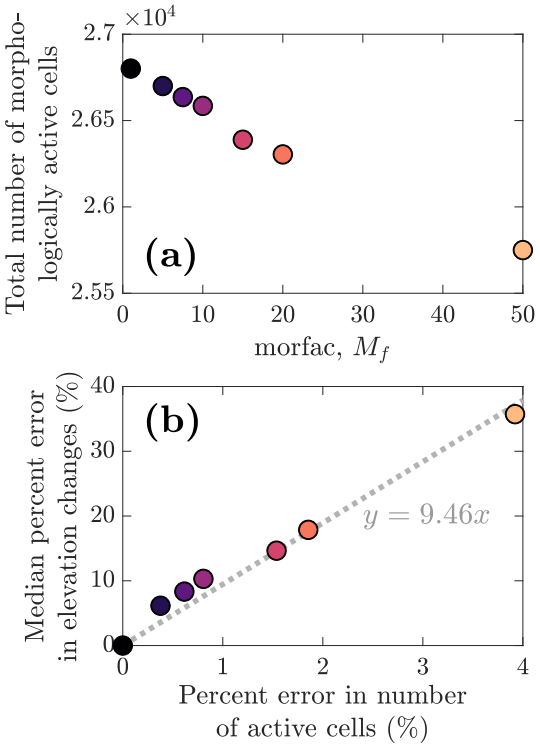

Fig. 9. (a) Variation in count of morphologically active grid cells (defined as cells with non-zero elevation change) with morfac and (b) variation in median percent error in elevation changes with percent error in active cell count. Colors in (b) represent M_f values indicated in (a).

(2016) with errors ranging from 0 − 51% for M_f=2 − 20. However, net volume change errors for our simulations range from 8 − 30%, while Williams et al. (2016) report net volume change errors upwards of 200%. That errors in signed volume changes are so similar, but errors in net volume changes differ by an order of magnitude is likely related the spatial scales considered. Our net volume changes are summed over approximately 70 km of river length whereas the results from Williams et al. (2016) represent only a 2.5 km length of river. Because the spatial domain here is large, there are a number of different channel planform types represented (e.g., meandering, braiding). Although we observed lower median elevation change errors in wider channel lengths, the high dynamism of braided reaches, such as those studied by Williams et al. (2016), may result in accumulation of a higher count of cells with erroneous elevation changes causing greater net errors. In our simulations, areas where this may be the case are offset by regions of less morphodynamism.

4.3. Effects of major tributary contributions

Large-scale morphodynamics require consideration of the channel networks that make up fluvial systems. This includes contributions of flow and sediment from tributaries and their interaction with the main channel at confluences. These contributions and interactions are often substantial and should be included in modeling domains. The use of morfac as we have implemented it and the inclusion of major tributaries complicates errors caused by morfac. Hydrodynamic and morphodynamics associated with test simulations of M_f=1 and M_f=15 are shown in Fig. 11. For the event simulated, the boundary hydrographs for the mainstem and two tributaries showed similar shapes and magnitudes. For M_f=1, where the flood wave propagates through the domain in less than 24 h (Fig. 11c), this resulted in a flood wave hydrograph that retained its shape as it propagated downstream (Fig. 11a). For M_f=15, however, the effective time lag in flood wave propagation causes the mainstem hydrographs and tributary hydrographs to become out of phase, exacerbating the attenuation of the flood wave (Fig. 11b and c). Consequently, M_f=15 errors increased from $\mathcal{O}(10\%)$ to $\mathcal{O}(100\%)$ downstream of tributary junctions when comparing the simulation results without tributaries to those including tributary contributions (Fig. 11d, cf. Fig. 7k). Tributary flow contributions, and associated timing, therefore, can contribute significantly to morfac-related morphodynamic errors. A potential solution to this would be to manually shift the tributary time-series to be in phase with the mainstem flood wave. However, this would require knowledge of the celerity error a priori.

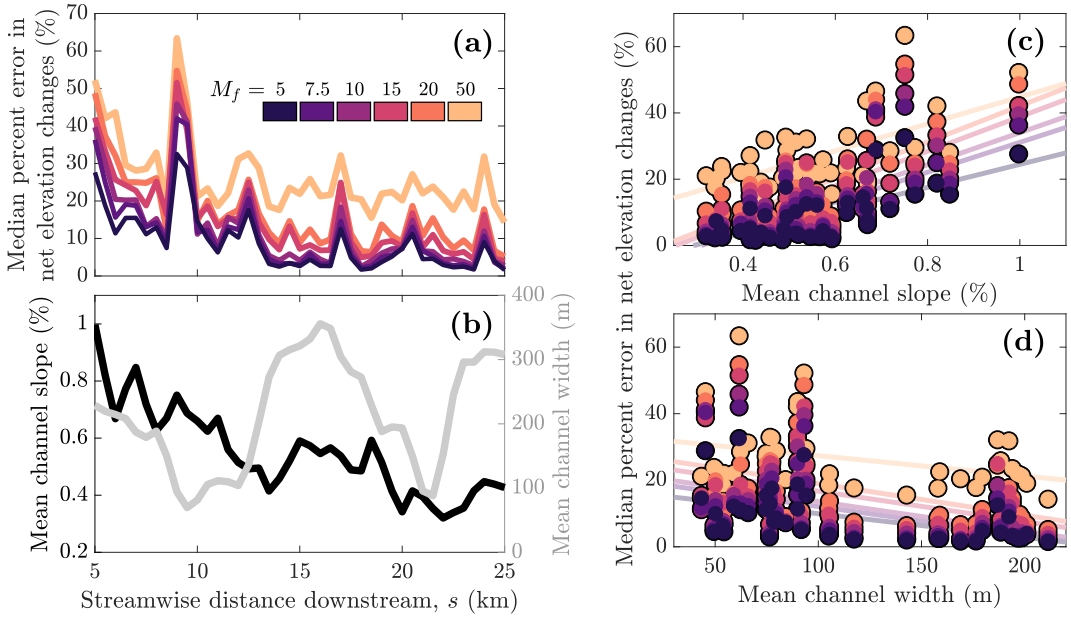

Fig. 10. (a) Downstream variation in median absolute percent error of net elevation changes, (b) downstream variation in mean channel slope and maximum reach-average channel width, (c) variation in error with mean channel slope, and (d) variation in error with mean channel width. Colors corresponding to M_f in (a) are consistent in (c) and (d) also.

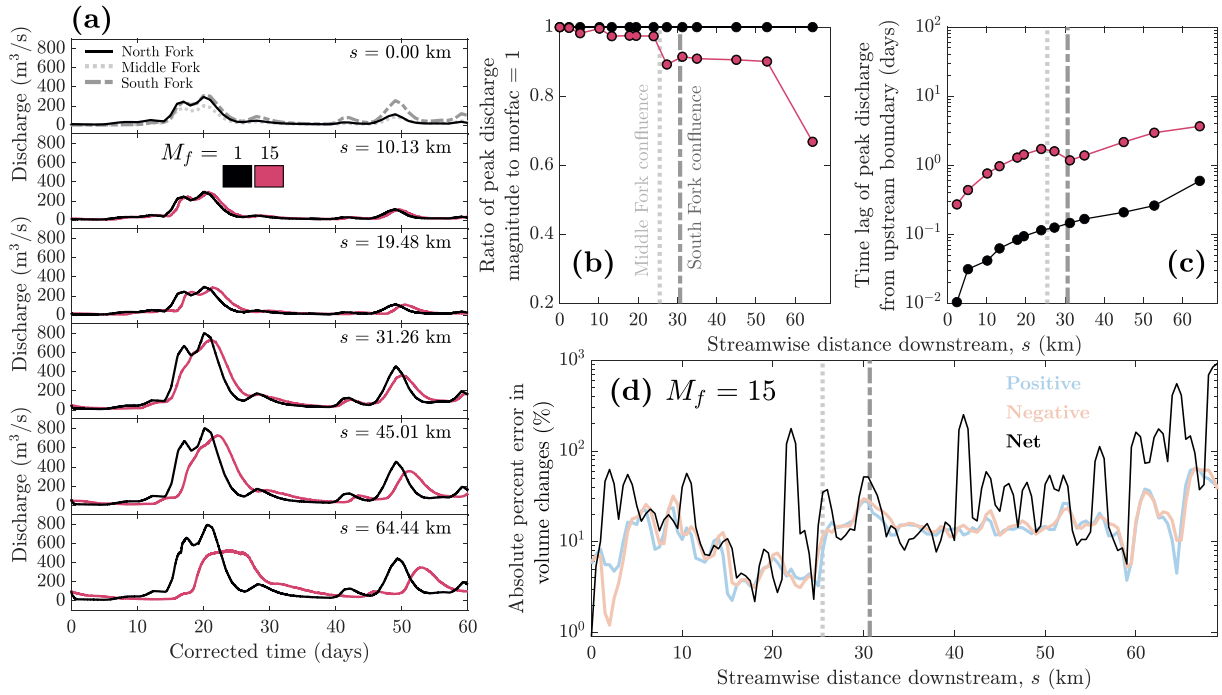

Fig. 11. Effect of M_f=15 coupled with the inclusion of tributary discharge. (a) Time-series discharge at several downstream locations, (b) ratio of peak discharge magnitude to M_f=1 discharge magnitude, (c) relative corrected time from upstream boundary to peak discharge, and (d) percent error in volume changes for positive (blue), negative (red), and net (black) values. In all plots the light gray dotted line corresponds to Middle Fork confluence (s=25 km) and the darker gray dash-dot line corresponds to South Fork confluence (s=30 km).

4.4. Relative importance of morfac-related errors in long time-scale simulations

It is worth noting that M_f is intended to be applied to much longer time-scale simulations than those conducted here, especially for coastal applications (Lesser et al., 2004). However, testing morfac values in our set-up for annual or decadal time periods is problematic because of the computational time needed for a simulation with no acceleration. The implications of morfac and a compressed upstream hydrograph on morphological changes on such longer time-scales still needs to be addressed, yet findings from this study suggest that even small morfac values for an event-scale simulation may lead to errors on the order of 10%. It is possible that errors would accumulate further and continue to increase with the length of the simulation, but it is also conceivable that errors may plateau after a time, or that longer term feedback may occur that modulate or compensate errors. If, for some reason, longer simulations result in less errors than shorter simulations, analysis should be limited to those longer time-scales, as our results suggest errors can be significant on the event time-scale.

Furthermore, error caused by uncertainty in input variables and parameterization of processes may be of similar order as the error in computations using morfac. Error sources may include: roughness parameterization, sediment transport relation, critical or reference Shields stress, active layer thickness, initial topography/bathymetry or grain sizes, and lateral slope effects (Schuurman et al., 2013; Beckers et al., 2017; Baar et al., 2019; van Dijk et al., 2019). For example, Schuurman et al., 2013 show that after > 15 months of simulation, braided river bar length is as affected by transverse bed slope parameter and bed roughness as morfac, and less affected by sediment transport relation. Bar height, braiding index, and active width, however, are relatively insensitive to morfac, while remaining sensitive to the other aforementioned parameters (Schuurman et al., 2013). For longer time-scale simulations, the selection of a bedload relation is likely to have major implications (Gomez and Church, 1989; Martin and Ham, 2005). If sediment transport measurements, or proxies, exist, formulas may be selected or modified to match observational data (e.g., Gaeuman et al., 2009). In the absence of field measurements, transport-formula-related uncertainty may overshadow morfac-related error in long-term simulations. Similarly, over long time-scales the uncertainty effects of transverse bed slope parameterization may be greater than morfac-related errors. Recent research by Baar et al. (2019) shows that the representation of slope effects on sediment transport direction and magnitude can have significant effects on simulated morphology. Also, the selection of lateral slope parameter may affect the computed morphology (hypsometry) much more than morfac values ranging from 5 to 100 (van Dijk et al., 2019).

Lack of surface or subsurface grain size data, or interpolation of data onto the numerical grid, such as topography and bathymetry, may also induced errors greater than or equal to the morfac-related errors reported here. For our results, insufficient simulation time for the highest morfac values gives rise to additional uncertainty in our analysis of the simulations presented here. For example, the second peak of the inflow hydrograph (~50 d at s=0 km in Fig. 4a) does not reach the downstream end of the domain (s=64.44 km) before the end of the simulation. However, because elevation changes continue to diminish with increasing morfac, and because the second inflow hydrograph peak is of substantially lower magnitude than the first peak, this uncertainty is not likely to have any effect on the analysis or conclusions presented here. Further research is necessary to identify the relative uncertainty contributions of morfac at this spatial scale alongside input parameters, transport relation selection, and representation of transverse slope effects. However, our results from simulations of 60 d show elevation errors $\mathcal{O}(10\%)$ for morfac values as low as two (Figs. 9b and 10a), suggesting much greater variability than simulations with steady flow (Kleinhans et al., 2008; Crosato et al., 2011). Along with the results of Williams et al. (2016), this suggests morfac errors on the same order of magnitude or greater than uncertainties associated with active layer formulation, grain size parameterization, and bedload relation selection. It is likely that errors will continue to accrue over longer time scales, as is the case in steady flow (Li, 2010), and therefore will continue to contribute to error/uncertainty on the same order of magnitude as the sources of uncertainties mentioned above.

4.5. Alternate methods for morphological acceleration

Additional methods exist for reducing computation times by exploiting the characteristic time differences between hydrodynamics and morphodynamics. For some natural systems, steady flow simulations may be sufficient in capturing long-term and/or large-scale morphodynamics. In such cases the use of a constant morfac is trivial. In other cases, varying discharge may be important, but the temporal rate of change is low such that a quasi-steady approximation may be sufficient (Yossef et al., 2008). A repeating, quasi-steady, schematized annual hydrograph may be produced from a discharge exceedance curve and morfac made to vary inversely with each discharge level (Yossef et al., 2008, 2016; Guerrero et al., 2015; Singh et al., 2017; Schuurman et al., 2018). Such a method can also be modified to generate a quasi-steady discharge regime considering smaller time-scales for cases of intra- or inter-annual variability (Huthoff et al., 2010; George et al., 2012; van Oorschot et al., 2015). Morphological acceleration may also be achieved by implementing an acceleration factor and updating morphology at a frequency M_f^{-1} that of the hydrodynamic calculations (Huang et al., 2008; Guerrero et al., 2015; Williams et al., 2016). However, this method will not result in as significant a reduction in computational time, because the hydrodynamic time-step is unaltered. If both variable discharge and unsteadiness are important, a characteristic hydrograph may be repeated in cycles and morfac applied in a way analogous to tidal cycles in coastal simulations. For example, an annual hydrograph simulated with a morfac of 10 would be equivalent to a 10-yr morphodynamic simulation. We are not aware of any published studies where such a method is employed or evaluated. Although morfac values ≥ 10 are widely used in steady flow fluvial morphodynamic modeling without noticeable effects, analysis of our results highlights the fact that caution should be used when applying a morfac in unsteady flow conditions.

5. Conclusions

We conducted a systematic test of the morphological acceleration factor to calculate large-scale fluvial morphodynamics. We tested M_f values of 5, 7.5, 10, 15, 20, and 50, comparing simulation results with those computed using no acceleration ($M_f = 1$). Our results show that hydrograph compression associated with morfac creates increasingly attenuative flood waves. The diminished peak flow magnitudes result in greater morphodynamic errors with increasing M_f values. Total median errors for for all test simulations are $\mathcal{O}(10\%)$ and are correlated to the number of morphologically active cells. Shallower channel slopes and wider channel widths show relatively low errors, indicating that for limited reaches the use of morfac may produce satisfactory results. The inclusion of tributary discharge increases errors downstream of the confluence because of the hydrograph phase-shift associated with effectively lower flood wave celerities in the mainstem. Additional methods that leverage the interactions between morfac and hydro-morphodynamics, such as a time-varying morfac or repeated characteristic discharge hydrograph, may reduce errors in simulated morphodynamics relative to no acceleration.

Declaration of competing interest

The authors declare that they have no known competing financial interests or personal relationships that could have appeared to influence the work reported in this paper.

Acknowledgments

This work was supported by National Science Foundation PREEVENTS Track 2: Integrated Modeling of Hydro-Geomorphic Hazards: Floods, Landslides and Sediment (ICER #1663859). We are grateful to Brian Collins for providing the shapefiles associated with the data presented in Collins and Sheikh (2004). We also thank Bert Jagers, Willem Ottevanger, and others at Deltares for sharing insights on Delft3D. Lidar data used to create model topography are downloadable from the Washington Lidar Portal (http://lidarportal.dnr.wa.gov). Measured bathymetry data are available as an interpolated raster at 3-foot resolution from the USGS ScienceBase-Catalog (https://doi.org/10.5066/F72B8W7M). Topnet model output used for discharge boundary conditions is available on HydroShare (https://doi.org/10.4211/hs.07c1b92dbc844234b9d9a3050cef3c4b). This manuscript has benefited from the comments of Richard Measures, an anonymous reviewer, and editor Scott Lecce.

References

Anderson, S.W., Grossman, E.E., 2017. Bathymetric DEM of the Lower Nooksack River, August 2015. U.S. Geological Survey data release. .
Anderson, S.W., Konrad, C.P., 2019. Downstream-propagating Channel Responses to Decadal-scale Climate Variability in a Glaciated River Basin. Journal of Geophysical Research, Earth Surface.
S. W. Anderson, C. P. Konrad, E. E. Grossman, C. A. Curran, Sediment storage and transport in the Nooksack River basin, northwestern Washington, 2006–15, U.S. Geological Survey, Scientific Investigations Report 2019–5008, 2019.
Baar, A.W., Albernaz, M.B., van Dijk, W.M., Kleinhans, M.G., 2019. Critical dependence of morphodynamic models of fluvial and tidal systems on empirical downslope sediment transport. Nat. Commun. 10.
Lower Nooksack Water Budget, Whatcom County. In: Bandaragoda, C., Greenberg, J., Dumas, M., Gill, P. (Eds.), WA: WRIA 1 Joint Board Http://wria1project.whatcomcounty.org/.
Bandaragoda, C., Greenberg, J., Dumas, M., 2019. LNWB Ch12-13 Existing and Historic Model Outputs - Data. HydroShare. .
Beckers, F., Noack, M., Wieprecht, S., 2017. Uncertainty analysis of a 2D sediment transport model: an example of the Lower River Salzach. J. Soils Sediments 18, 3133–3144.
Bertschi, R.G., 1993. Channel Changes and Flood Frequency on the Upper Main Stem of the Nooksack River. Washington, Master's thesis, Western Washington University, Whatcom County Https://cedar.wwu.edu/wwuet/717/.
Chavarrías, V., Stecca, G., Siviglia, A., Blom, A., 2019. A regularization strategy for modeling mixed-sediment river morphodynamics. Adv. Water Resour. 127, 291–309.
Colebrook, C.F., 1939. Turbulent flow in pipes, with particular reference to the transition region between smooth and rough pipe laws. Journal of the Institution of Civil Engineers 11, 133–156.
Colebrook, C.F., White, C.M., 1937. Experiments with fluid friction in roughened pipes, Proceedings of the Royal Society of London. Series A-Mathematical and Physical. Sciences 161, 367–381.
M. R. Collings, R. W. Smith, G. T. Higgins, The Hydrology of Four Streams in Western Washington as Related to Several Pacific Salmon Species, U.S. Geological Survey, Water-Supply Paper 1986, 1972.
Collins, B., Sheikh, A., 2004. Historical ChannelLocations of the Nooksack River. Whatcom County Public Works Department Https://www.whatcomcounty.us/2572/Completed-Plans-Nooksack-River.
Crosato, A., Mosselman, E., Beidmariam Desta, F., Uijttewaal, W.S.J., 2011. Experimental and numerical evidence for intrinsic nonmigrating bars in alluvial channels. Water Resour. Res. 47.
Dastgheib, A., Roelvink, J.A., Wang, Z.B., 2008. Long-term process-based morphological modeling of the Marsdiep Tidal Basin. Mar. Geol. 256, 90–100.
David, C.H., Maidment, D.R., Niu, G.-Y., Yang, Z.-L., Habets, F., Eijkhout, V., 2011. River network routing on the NHDPlus dataset. J. Hydrometeorol. 12, 913–934.
Deltares, 2014. Delft3D-FLOW, User Manual: Simulation of Multi-Dimensional Hydrodynamic Flows and Transport Phenomena, Including Sediments, Deltares. Delft, The Netherlands Http://oss.deltares.nl/documents/183920/185723/Delft3D-FLOW_User_Manual.pdf.
van Dijk, W.M., Schuurman, F., Van de Lageweg, W.I., Kleinhans, M.G., 2014. Bifurcation instability and chute cutoff development in meandering gravel-bed rivers. Geomorphology 213, 277–291.
van Dijk, W.M., Hiatt, M.R., van der Werf, J.J., Kleinhans, M.G., 2019. Effects of shoal margin collapses on the morphodynamics of a sandy estuary. Journal of Geophysical Research: Earth Surface 124, 195–215.
Duró, G., Crosato, A., Tassi, P., 2016. Numerical study on river bar response to spatial variations of channel width. Adv. Water Resour. 93, 21–38.
Edmonds, D.A., 2012. Stability of backwater-influenced river bifurcations: a study of the Mississippi-Atchafalaya system. Geophys. Res. Lett. 39.
Fenton, J.D., 2019. Flood routing methods. J. Hydrol. 570, 251–264.
Gaeuman, D., Andrews, E.D., Krause, A., Smith, W., 2009. Predicting fractional bed load transport rates: application of the wilcock-crowe equations to a regulated gravel bed river. Water Resour. Res. 45.
Geological Survey, U.S., 2018. Water Data for the Nation. Http://waterdata.usgs.gov/nwis/.
George, D.A., Gelfenbaum, G., Stevens, A.W., 2012. Modeling the hydrodynamic and morphologic response of an estuary restoration. Estuar. Coasts 35, 1510–1529.
Gomez, B., Church, M., 1989. An assessment of bed load sediment transport formulae for gravel bed rivers. Water Resour. Res. 25, 1161–1186.
Guerrero, M., Latosinski, F., Nones, M., Szupiany, R.N., Re, M., Gaeta, M.G., 2015. A sediment fluxes investigation for the 2-D modelling of large river morphodynamics. Adv. Water Resour. 81, 186–198.

Huang, J., Borthwick, A.G., Soulsby, R.L., 2008. One-dimensional modelling of fluvial bed morphodynamics. J. Hydraul. Res. 46, 636–647.
Huthoff, F., van Vuren, S., Barneveld, H.J., Scheel, F., 2010. On the importance of discharge variability in the morphodynamic modeling of rivers. A. Dittrich, K. Koll, J. Aberle, P. Geisenhainer (Eds.), River Flow. Braunschweig, Germany, pp. 985–991.
Ikeda, S., 1984. Closure to "lateral bed load transport on side slopes" by syunsuke ikeda. november, 1982. J. Hydraul. Eng. 110, 200–203.
Kalkwijk, J.P.T., Booij, R., 1986. Adaptation of secondary flow in nearly-horizontal flow. J. Hydraul. Res. 24, 19–37.
KCM, Inc, 1995. Lower Nooksack River Comprehensive Flood Hazard Management Plan. Whatcom County Transportation Services Department, Sediment Supply and Transport Https://www.whatcomcounty.us/DocumentCenter/View/25545/Sediment-Supply-and-Transport.
Kleinhans, M.G., Jagers, H.R.A., Mosselman, E., Sloff, C.J., 2008. Bifurcation dynamics and avulsion duration in meandering rivers by one-dimensional and three-dimensional models. Water Resour. Res. 44.
Lesser, G.R., 2009. An approach to medium-term coastal morphological modelling, Ph.D. thesis, Delft University of Technology. UNESCO-IHE Institute for Water Education Http://resolver.tudelft.nl/uuid:27a1ffa0-580e-4eae-907b-ce6f901e652e.
Lesser, G.R., Roelvink, J.A., Van Kester, J.A.T.M., Stelling, G.S., 2004. Development and validation of a three-dimensional morphological model. Coastal Engineering 51, 883–915.
Li, L., 2010. A Fundamental Study of theMorphological Acceleration Factor. Delft University of Technology, Master's thesis Http://resolver.tudelft.nl/uuid:2780f537-402b-427a-9147-b8652279a83e.
Maaß, A.-L., Schüttrumpf, H., 2018. Long-term effects of mining-induced subsidence on the trapping efficiency of floodplains. Anthropocene 24, 1–13.
Martin, Y., Ham, D., 2005. Testing bedload transport formulae using morphologic transport estimates and field data: lower Fraser river, British Columbia. Earth Surf. Process. Landf. 30, 1265–1282.
Moerman, E., 2011. Long-termMorphological Modelling of the Mouth of the Columbia River. Delft University of Technology,Master's thesis Http://resolver.tudelft.nl/uuid:0a39e67c-ec24-4264-b523-d3ece34f9da8.
Mosselman, E., Le, T.B., 2016. Five common mistakes in fluvial morphodynamic modeling. Adv. Water Resour. 93, 15–20.
Nicholas, A.P., Ashworth, P.J., Sambrook Smith, G.H., Sandbach, S.D., 2013. Numerical simulation of bar and island morphodynamics in anabranching megarivers. Journal of Geophysical Research: Earth Surface 118, 2019–2044.
Northwest Hydraulics Consultants, 1989. Nooksack River Sedimentation Model Development. Whatcom County Engineering Services.
van Oorschot, M., Kleinhans, M., Geerling, G., Middelkoop, H., 2015. Distinct patterns of interaction between vegetation and morphodynamics. Earth Surf. Process. Landf. 41, 791–808.
Ranasinghe, R., Swinkels, C., Luijendijk, A., Roelvink, D., Bosboom, J., Stive, M., Walstra, D., 2011. Morphodynamic upscaling with the MORFAC approach: dependencies and sensitivities. Coast. Eng. 58, 806–811.
Schuurman, F., Marra, W.A., Kleinhans, M.G., 2013. Physics-based modeling of large braided sand-bed rivers: bar pattern formation, dynamics, and sensitivity. Journal of Geophysical Research: Earth Surface 118, 2509–2527.
Schuurman, F., Ta, W., Post, S., Sokolewicz, M., Busnelli, M., Kleinhans, M., 2018. Response of braiding channel morphodynamics to peak discharge changes in the upper yellow river. Earth Surf. Process. Landf. 43, 1648–1662.
Singh, U., Crosato, A., Giri, S., Hicks, M., 2017. Sediment heterogeneity and mobility in the morphodynamic modelling of gravel-bed braided rivers. Adv. Water Resour. 104, 127–144.
Stark, J., 2012. The Influence of Dredging Activities on the Morphological Development of the ColumbiaRiver Mouth. Delft University of Technology, Master's thesis Http://resolver.tudelft.nl/uuid:e5d65bb4-5aef-432e-b6a2-871fb22f0de4.
van der Wegen, M., Roelvink, J.A., 2008. Long-term morphodynamic evolution of a tidal embayment using a two-dimensional, process-based model. Journal of Geophysical Research: Oceans 113.
van der Wegen, M., Wang, Z.B., Savenije, H.H.G., Roelvink, J.A., 2008. Long-term morphodynamic evolution and energy dissipation in a coastal plain. tidal embayment, Journal of Geophysical Research: Earth Surface 113.
Westbrook, M., 1987. Wells Creek Hydroelectric Project (FERC No. 4682) Erosion and Sedimentation Field Study Report. Western Powere, Inc.
Wilcock, P.R., Crowe, J.C., 2003. Surface-based transport model for mixed-size sediment. J. Hydraul. Eng. 129, 120–128.
Williams, R.D., Measures, R., Hicks, D.M., Brasington, J., 2016. Assessment of a numerical model to reproduce event-scale erosion and deposition distributions in a braided river. Water Resour. Res. 52, 6621–6642.
WSI, Nooksack River Basin LiDAR: Technical Data Report – Delivery 2, 2013. Https://pugetsoundlidar.ess.washington.edu/lidardata/proj_reports/Nooksack_River_Basin_LiDAR_Delivery
M. F. M. Yossef, H. R. A. Jagers, S. Van Vuren, J. Sieben, Innovative techniques in modelling large-scale river morphology, in: M. Altinakar, M. A. Kokpinar, Y. Darama, B. Yegen, N. B. Harmancioglu (Eds.), River Flow 2008, Izmir, Turkey.
M. F. M. Yossef, A. Becker, G. Deák, Modelling large scale and long term morphological response to engineering interventions at river bifurcation, in: G. Constantinescu, H. Garcia, D. Hanes (Eds.), River Flow 2016, CRC Press, pp.1352–1359.